

# Instantaneous planar pressure determination from PIV in turbulent flow

R. de Kat · B. W. van Oudheusden

Received: 8 March 2011 / Revised: 3 September 2011 / Accepted: 19 November 2011 / Published online: 7 December 2011  
© The Author(s) 2011. This article is published with open access at Springerlink.com

**Abstract** This paper deals with the determination of instantaneous planar pressure fields from velocity data obtained by particle image velocimetry (PIV) in turbulent flow. The operating principles of pressure determination using a Eulerian or a Lagrangian approach are described together with theoretical considerations on its expected performance. These considerations are verified by a performance assessment on a synthetic flow field. Based on these results, guidelines regarding the temporal and spatial resolution required are proposed. The interrogation window size needs to be 5 times smaller than the flow structures and the acquisition frequency needs to be 10 times higher than the corresponding flow frequency (e.g. Eulerian time scales for the Eulerian approach). To further assess the experimental viability of the pressure evaluation methods, stereoscopic PIV and tomographic PIV experiments on a square cylinder flow ( $Re_D = 9,500$ ) were performed, employing surface pressure data for validation. The experimental results were found to support the proposed guidelines.

## 1 Introduction

The pressure field in a fluid is of great interest in both fluid mechanics and engineering. Combined with the velocity field, the pressure field gives a complete description of the (incompressible) flow dynamics. Furthermore, the pressure field is the main contributor to the aerodynamic loading of bodies immersed in the fluid. Current techniques focus on the determination of surface pressure and integral loads by point pressure and force balance measurements. However, so far, no method can instantaneously measure both the velocity and pressure field.

Considerable effort has been put into deriving forces from velocity fields (e.g. PIV data) and even though the pressure field is an integral part of forces that are exerted on the body immersed in the fluid, most efforts try to avoid calculating the pressure explicitly (see e.g. Noca et al. 1999).

With the development and success of nonintrusive flow diagnostic techniques, such as particle image velocimetry (PIV, Raffel et al. 2007) in particular, it might be possible to determine instantaneous aerodynamic loads. PIV has already proven its capability in characterizing instantaneous velocity fields and derived quantities such as vorticity, whereas its use in determining the instantaneous pressure field remains relatively unexplored. Several studies have addressed different approaches to derive (mean) pressure from PIV velocity data.

Gurka et al. (1999) derived from a steady velocity field the pressure distribution in a channel flow. Concurrently, Baur and Köngeter (1999) explored determination of instantaneous pressure from time-resolved data, addressing local pressure reduction in the vortices shed from a wall-mounted obstacle, using a two-dimensional (2D) approach. Hosokawa et al. (2003) used PIV data to obtain pressure

---

This work is supported by the dutch technology foundation, STW, grant 07645.

---

R. de Kat · B. W. van Oudheusden  
Department of Aerospace Engineering, Delft University  
of Technology, Kluyverweg 1, 2629 HS Delft, The Netherlands  
e-mail: B.W.vanOudheusden@tudelft.nl

*Present Address:*  
R. de Kat (✉)  
Engineering and the Environment, University of Southampton,  
Highfield, Southampton SO17 1BJ, UK  
e-mail: R.de-Kat@soton.ac.uk

distributions around single bubbles, while Fujisawa et al. (2005) derived pressure fields around and fluid forces on a circular cylinder. Liu and Katz (2006) show the application of pressure determination from PIV on a cavity flow. Fujisawa et al. (2006) apply pressure reconstruction on a micro channel using micro-PIV data. Pressure evaluation from PIV data has even found its extension into the compressible regime as demonstrated by van Oudheusden (2008).

Although several studies have explored the possibility to obtain the pressure field, relatively little attention has been given to the systematic analysis of the key experimental aspects that determine the accuracy of pressure determination. Essential elements are the spatial and temporal resolution of the velocity measurements, as well as the different approaches (Eulerian or Lagrangian) to determine fluid acceleration and the subsequent integration of the pressure gradient.

Charonko et al. (2010) review different approaches in a Eulerian basis applied on two ideal sample flow fields and show an application to an oscillating flow in a diffuser. Violato et al. (2010) compare an Eulerian approach with a Lagrangian approach on a rod-aerofoil configuration.

As the velocity data used as input are primarily obtained from planar PIV, most of these studies are hampered by the restriction of 2D (average) flow or necessarily making 2D flow assumptions, where it is not obvious what the impact of this assumption can be. Also, no complete comprehensive analysis of the experimental parameters (PIV settings, such as interrogation window size, overlap factors, etc.) that will determine the success of pressure PIV has been reported yet. Charonko et al. (2010) give an overview of different integration approaches and of the influence of temporal and spatial resolution, but do not include the filtering effect that PIV has on both the velocity field and the measurement noise (in combination with overlap, this will lead to correlated noise, whereas they use uncorrelated noise). They also did not include a Lagrangian approach in their comparison, while comparisons of the Eulerian and Lagrangian form showed that the Lagrangian approach is less prone to measurement noise (Violato et al. 2010). Christensen and Adrian (2002) found that for their advecting turbulence experiment, the material acceleration was about one order of magnitude smaller than the time change of the velocity at one point, which would also promote the use of a Lagrangian approach. On the other hand, Jakobsen et al. (1997) found that for waves impinging on a vertical wall, their Lagrangian approach had limitations and showed bias effects, resulting in a worse performance than their Eulerian approach. These contradictory results show the need of a direct comparison of the two approaches.

Furthermore, previous efforts to validate the pressure determination have given little attention to advecting

vortices, whereas they are characteristic features occurring in many fluid dynamic problems (e.g. turbulence and vortex shedding). Also, a direct experimental validation for instantaneous pressure is still lacking. In this paper, our aim is to address these above-mentioned questions.

This paper assesses the performance of a Eulerian and Lagrangian approach for turbulent flows. First, the operating principles are introduced together with theoretical considerations to estimate the frequency response (both truncation and precision effects) and the limitations of the approaches. Next, the approaches are tested on synthetic data consisting of an advecting Gaussian vortex from which the influences of different flow parameters are determined (e.g. advective velocity and vortex strength). From both the theoretical considerations and the assessment on the synthetic flow field, conclusions regarding the proper application of the approaches will be given. To show the experimental viability of the pressure evaluation methods, stereoscopic PIV (stereo-PIV) and tomographic PIV (tomo-PIV, Elsinga et al. 2006) experiments on a square cylinder were performed, employing surface pressure data for validation. Pressure-dominated flows around bluff bodies pose relevant and challenging test cases for pressure evaluation from planar PIV, due to the complex time-evolving three-dimensional (3D) nature of the flow field, especially at moderate to high Reynolds numbers (see e.g. Williamson 1996). The current experiments were performed at a Reynolds number where transition of the shear layer is present and the near-wake shows significant 3D flow structures (see de Kat et al. 2009a, b).

## 2 Pressure evaluation from PIV

Pressure evaluation from PIV velocity data involves two steps. First, the pressure gradient is evaluated from locally applying the momentum equation in differential form. The second step is to spatially integrate the pressure gradient to obtain the pressure field. These steps can be performed in different ways, where each way has its own limitations as will be described in this section.

### 2.1 Operating principle

The incompressible momentum equation for 3D flow can give the relation between the pressure gradient and the velocity data in two different forms: the Eulerian form or the Lagrangian form, given as

$$\begin{aligned}\nabla p &= -\rho \left\{ \frac{\partial \mathbf{u}}{\partial t} + (\mathbf{u} \cdot \nabla) \mathbf{u} - \nu \nabla^2 \mathbf{u} \right\} \quad \text{or} \\ \nabla p &= -\rho \left\{ \frac{D\mathbf{u}}{Dt} - \nu \nabla^2 \mathbf{u} \right\},\end{aligned}\tag{1}$$

respectively. Although the viscous term can be determined, its effect on the pressure gradient can generally be neglected and will therefore be omitted in the following discussion (see van Oudheusden et al. 2007, who found the viscous contribution to be two orders of magnitude smaller for a similar Reynolds number).

In case of 2D flow, planar time-resolved PIV will suffice for determining the pressure gradients, but for 3D flow, all components of the velocity and velocity gradient are needed, which may be accomplished by a time-resolved tomographic PIV procedure, for example see Schröder et al. (2008).

We will concentrate on the procedure to determine the pressure in a cross-sectional plane in the flow. To evaluate the pressure in the plane (here defined as the  $x$ - $y$ -plane), only the two in-plane pressure gradient components are needed. The reader should note, however, that these in-plane pressure gradient components contain in- and out-of-plane components of velocity and velocity gradient.

To obtain pressure, the pressure gradient can be spatially integrated using a direct spatial integration of the pressure gradient or using a Poisson formulation. In the latter approach, the in-plane divergence of the pressure gradient is taken Eq. 2 and subsequently integrated by a Poisson solver. The in-plane divergence of a vector function,  $\mathbf{g}$ , is  $\nabla_{xy} \cdot \mathbf{g} = \partial g_x / \partial x + \partial g_y / \partial y$ , where  $g_x$  and  $g_y$  are the components in  $x$ - and  $y$ -direction, respectively.

$$\nabla_{xy} \cdot \nabla p = \frac{\partial^2 p}{\partial x^2} + \frac{\partial^2 p}{\partial y^2} = -\rho f_{xy} \quad (2)$$

where  $f_{xy}$  is a function of the velocity field obtained by taking the in-plane divergence of Eq. 1 and dividing by  $-\rho$ , resulting in

$$f_{xy} = f_{2D} + f_{3D} = \left\{ \left( \frac{\partial u}{\partial x} \right)^2 + 2 \frac{\partial v}{\partial x} \frac{\partial u}{\partial y} + \left( \frac{\partial v}{\partial y} \right)^2 \right\} + \left\{ \frac{\partial (\nabla_{xy} \cdot \mathbf{u})}{\partial t} + (\mathbf{u} \cdot \nabla) (\nabla_{xy} \cdot \mathbf{u}) + \frac{\partial w}{\partial x} \frac{\partial u}{\partial z} + \frac{\partial w}{\partial y} \frac{\partial v}{\partial z} \right\} \quad (3)$$

where  $f_{2D}$  indicates the part caused by the in-plane part of the flow and  $f_{3D}$  indicates the additional terms for 3D flow.

Now, even for 3D flow, most of the extra terms that appear can be extracted from planar-PIV data, see Eq. 3. The additional 3D flow contributions contain the in-plane divergence of the velocity, which can be derived from planar PIV data. 3D velocity information is needed for the parts containing an out-of-plane gradient.

## 2.2 Numerical implementation

For the numerical implementation, we choose to split the problem in two. First, we determine the pressure gradient

field and subsequently, we determine the pressure field by integrating the pressure gradient field. This makes it easier to pinpoint where the errors in the pressure determination arise. In the following discussion,  $\Delta t$  refers to the vector field time separation ( $1/f_{acq}$ ) as distinct from the laser pulse time separation for which we will use  $\delta t$ .

The Pressure gradient can be computed in two different ways: a Lagrangian form where all quantities are evaluated with respect to an element moving with the flow and in a Eulerian form where everything is taken relative to a fixed spatial location. For the Eulerian approach, we use second-order central finite differences in space and time, as expressed by

$$\frac{\partial u}{\partial x}(x, y, z, t) = \frac{u(x+h, y, z, t) - u(x-h, y, z, t)}{2h} + O(h^2) \quad (4)$$

$$\frac{\partial u}{\partial t}(x, y, z, t) = \frac{u(x, y, z, t + \Delta t) - u(x, y, z, t - \Delta t)}{2\Delta t} + O(\Delta t^2), \quad (5)$$

respectively.  $u$  is the velocity component in  $x$ -direction,  $h$  is the grid spacing, and  $\Delta t$  is the time separation between consecutive velocity fields. The description of space and time is therefore not linked in computation or formulation (see Eq. 1).

For the Lagrangian approach, we need to reconstruct the fluid-parcel trajectory. In the present study, the fluid trajectory is reconstructed using a pseudo-tracking approach, which is derived from velocity fields rather than particle locations (see Liu and Katz 2006). A second-order fluid path is reconstructed using an iterative approach (indicated by the superscript  $k$ ) given by

$$\mathbf{x}_p^k(t, \tau) = \mathbf{x} + \mathbf{u}(\mathbf{x}, t)\tau + \frac{1}{2} \frac{D\mathbf{u}^k}{Dt}(\mathbf{x}, t)\tau^2 \quad (6)$$

$$\frac{D\mathbf{u}^{k+1}}{Dt}(\mathbf{x}, t) = \frac{\mathbf{u}(\mathbf{x}_p^k(t, \Delta t), t + \Delta t) - \mathbf{u}(\mathbf{x}_p^k(t, -\Delta t), t - \Delta t)}{2\Delta t} \quad (7)$$

where  $\mathbf{x}_p$  is the particle location. Equation 6 is the second-order expansion of the particle location with time interval  $\tau$  relative to time instance  $t$ .

Although for the Lagrangian form, the description of space and time seems not to be linked, based on the formulation in Eq. 1, it is clearly linked in the computation Eq. 6.

The pressure gradient field is consequently determined using Eq. 1. Both approaches use linear forward or backward schemes at domain edges.

Pressure integration is done by a Poisson solver that solves the in-plane Poisson formulation Eq. 2 directly using a standard 5-point scheme (second-order central

differences) with the forcing term determined as given in Eq. 8.

$$-\rho f_{xy} = \frac{\partial}{\partial x} \left( \frac{\partial p}{\partial x} \Big|_{\text{PIV}} \right) + \frac{\partial}{\partial y} \left( \frac{\partial p}{\partial y} \Big|_{\text{PIV}} \right) \quad (8)$$

To verify the proper working of this approach, we compared it to two alternative approaches for the integration of the pressure gradient: the omnidirectional integration approach used by Liu and Katz (2006) and a least-squares approach. A third approach, a direct spatial integration approach, was tested (see de Kat et al. 2008), but was excluded from this comparison because of its unfavourable directional dependence (see van Oudheusden 2008).

The differences in peak and noise response of the methods were found to be well below 1%, when tested on a stationary Gaussian vortex (see Sect. 3) on a grid of  $60 \times 90$  points. Furthermore, Charonko et al. (2010) found that when sufficiently sampled, different integration techniques give adequate results, even for different inputs (e.g. neglecting parts in Eq. 3). Based on these findings, the use of the Poisson approach is verified to be adequate for the following analyses.

*Boundary conditions* are enforced on all edges of the pressure evaluation domain and consist of a reference boundary condition in a point or domain (pressure is prescribed) and Neumann conditions (pressure gradient is prescribed) on the remaining edges. The reference boundary condition ideally would be placed in the inviscid outer flow, where the Bernoulli equation can be used. However, due to the limited measurement domain of PIV, the boundary conditions need to be enforced within the disturbed flow domain. To correct for this, the reference pressure is computed with an extended version of the Bernoulli equation that holds for an irrotational inviscid unsteady advective flow with small mean velocity gradients as given by

$$p + \frac{1}{2} \rho (\bar{\mathbf{u}} \cdot \bar{\mathbf{u}} + \mathbf{u}' \cdot \mathbf{u}') = p_\infty + \frac{1}{2} \rho V_\infty^2 \quad (9)$$

where  $\bar{\mathbf{u}}$  is the mean velocity and  $\mathbf{u}'$  is the fluctuation around the mean. The Neumann boundary conditions make use of Eq. 1 and are implemented by estimating the value of a point outside the domain (a ghost point) by using the gradient at the point on the boundary for extrapolation and thereby completing the 5-point scheme.

### 2.3 Frequency response

A key feature of an experimental technique used to measure turbulent flow is its frequency response. The frequency response of the measurement procedure and subsequent data analysis are affected in both space and

time by truncation and precision errors. The influence of the truncation error is estimated using (simple) theoretical considerations. The influence of the precision error is estimated using linear error propagation.

Although we set out to start from a velocity field with its corresponding uncertainty, we need to know how PIV filters the velocity field and the noise on it, in order to know what the starting point of the pressure derivation is. PIV acts similar to a moving average (see e.g. Schrijer and Scarano 2008, who also show improvements can be achieved with iterative schemes), resulting in a response (Fig. 1) to a 2D signal as given by

$$T_{\text{PIV}, 2\text{D}} = \text{sinc}^2 \left( \frac{WS}{\lambda_x} \right) \quad (10)$$

where  $T_{\text{PIV}, 2\text{D}}$  denotes the transfer function of PIV to a 2D signal,  $\text{sinc}(x) = \sin(\pi x)/\pi x$ ,  $WS$  is the interrogation window size, and  $\lambda_x$  is the spatial wavelength of the input signal. Foucaut et al. (2004) show that noise is also affected by this low-pass filter behaviour.

PIV also has a limited temporal response, which is related to the laser pulse time separation,  $\delta t$ , and restricts the frequencies of flow phenomena that can be captured in individual velocity fields. This, however, is generally less restrictive than the limitation by the acquisition frequency ( $\Delta t \geq \delta t$ ) and we will therefore focus on the influence of the acquisition frequency.

The current implementation of the determination of the pressure gradient field involves taking central finite differences. These central finite differences act as a low-pass filter due to the truncation error (see e.g. Foucaut and Stanislas 2002), with a response given in Eq. 11 (Fig. 1).

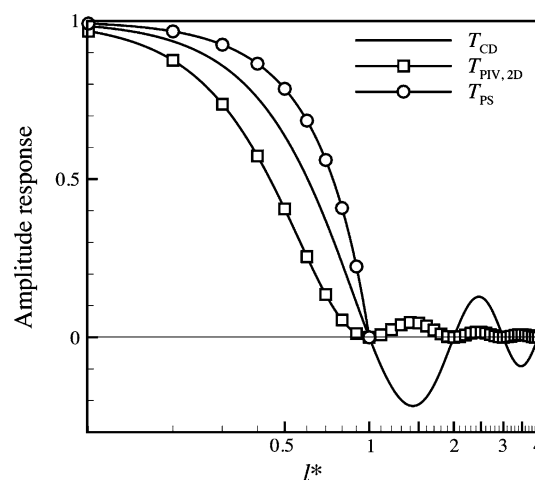


**Fig. 1** Amplitude response of PIV, central finite differences (CD), and the Poisson solver (PS). PIV:  $l^* = WS/\lambda_x$ ; CD and PS:  $l^* = 2h/\lambda_x$ . PS is shown till  $l^* = 1$ , which is the Nyquist limit of PS and CD

$$T_{\text{CD}} = \text{sinc}\left(\frac{2h}{\lambda_x}\right) \quad (11)$$

where  $T_{\text{CD}}$  denotes the transfer function of the central finite differences,  $h$  is the grid spacing. When applied in time the filter response is the same, i.e. replace  $h$  with  $\Delta t$  and  $\lambda_x$  with  $\lambda_t$ .

A numerical test and theoretical analysis indicates also that the Poisson solver acts as a low-pass filter with an amplitude response as given in Eq. 12 (Fig. 1).

$$T_{\text{PS}} = \frac{1 + \cos\left(\pi \frac{2h}{\lambda_x}\right)}{2 \cdot \text{sinc}\left(\frac{2h}{\lambda_x}\right)} \quad (12)$$

where  $T_{\text{PS}}$  denotes the transfer function of the Poisson solver.

For the pressure derived using the Eulerian form of the pressure gradient, this means the filter due to the central finite differences acts in space and time separately with an additional effect of the filter of the Poisson solver in space. When using the Lagrangian form of the pressure gradient, the low-pass filter due to the central finite differences only acts in time and the filter of the Poisson solver in space. However, for the Lagrangian approach, the reconstruction of the trajectory of the fluid-parcel path also has an additional dependency on the spatial frequency response (see Eq. 6).

Violato et al. (2010) state the temporal limitation of a Eulerian approach to be related to the acceleration being measured on the same structure, leading to the expression given by

$$\Delta t_{\text{Eul}} < \frac{1}{4} \frac{\lambda_x}{U_a} \quad (13)$$

where  $\Delta t_{\text{Eul}}$  is the time separation between consecutive velocity fields for the Eulerian approach,  $\lambda_x$  is the spatial wavelength, and  $U_a$  is the advective velocity.

However, this is only a part of the terms needed for the pressure gradient (see Eq. 1) and therefore does not state how strong the impact of this improper sampling will be. Following similar reasoning, i.e. a vortex should not exceed half a turn during the evaluation of the material acceleration, an equivalent expression can be derived for the temporal limitation of the Lagrangian approach,

$$\Delta t_{\text{Lag}} < \frac{1}{4} \frac{2\pi r}{V_\theta} \quad (14)$$

where  $\Delta t_{\text{Lag}}$  is the time separation between consecutive velocity fields for the Lagrangian approach,  $r$  is the radius, and  $V_\theta$  is the tangential velocity.

Here, the expression is linked directly to the pressure gradient and its effect is expected to influence the complete domain. Also, the domain should be large enough for the

fluid path to be reconstructed. However, it is not possible to accurately capture these effects in simple theoretical considerations, and therefore, they will be assessed on a synthetic flow field in Sect. 3.

To have an estimate for the sensitivity to noise (precision error) of both approaches, we follow a linear error propagation procedure as laid down by Kline and McClintock (1953) (see e.g. Stern et al. 1999, for a more thorough exposition). The error is assumed to be uncorrelated and to have a normal distribution. The error on a single sample can be estimated by the RMS value of the noise of the measurement tool, and the error on a derived quantity can then be estimated as the root of the sum of the square of the uncertainties of the samples where it was derived from multiplied by their respective sensitivity. The noise propagation from the velocity field to the pressure field for the Eulerian form gives

$$\varepsilon_{p_{\text{Eul}}} \propto \varepsilon_u \sqrt{\frac{h^2}{2\Delta t^2} + |\nabla u|^2 h^2 + \frac{|\mathbf{u}|^2}{2}} \quad (15)$$

where  $\varepsilon_{p_{\text{Eul}}}$  is the (estimated RMS) error for the pressure based on the Eulerian approach,  $\varepsilon_u$  is the noise on the velocity,  $h$  is the grid spacing,  $\Delta t$  is the velocity field time separation,  $|\nabla u|$  is the magnitude of the gradient of the streamwise component of the velocity, and  $|\mathbf{u}|$  is the velocity magnitude.

For the estimation of the noise sensitivity of the Lagrangian method, the fluid path reconstruction is simplified and taken to be linear (i.e. Eqs. 6, 7 are only used once). The result of the noise propagation then is

$$\varepsilon_{p_{\text{Lag}}} \propto \varepsilon_u \sqrt{\frac{h^2}{2\Delta t^2} + \frac{|\nabla u|^2 h^2}{2}} \quad (16)$$

where  $\varepsilon_{p_{\text{Lag}}}$  is the error for the pressure based on the Lagrangian approach.

These results indicate that when the (advective) velocity of the flow is small (with respect to the other terms in Eqs. 15, 16), both methods will react similarly to noise, whereas when the (advective) velocity is large, the Eulerian approach will suffer, while the Lagrangian approach remains insensitive.

Due to the nonlinearity (with respect to the velocity field) of the pressure gradient determination, the exact behaviour of both methods is not available. Also, the noise propagation estimation is limited to uncorrelated noise, whereas Foucaut et al. (2004) show that the (spatial) scales in the noise are affected by the PIV processing, especially apparent when using higher overlap factors (OF). Furthermore, the filtering effect of PIV is known to be different for 1 and 2D signals (see e.g. Schrijer and Scarano 2008).



Nevertheless, the considerations presented in this section provide a good indication of the parameters that will influence the performance of the pressure determination from PIV and what effect they may have. In summary, the Eulerian approach is expected to be more sensitive to noise and advective motion, whereas the Lagrangian should have difficulties capturing rotational flow, because this complicates the flow path reconstruction.

To substantiate and quantify these theoretical considerations on the performance of pressure determination, different methods are applied to a synthetic flow field, where the input velocity field has a known pressure distribution.

### 3 Performance assessment on a synthetic flow field

Vortices are arguably the most relevant flow structures occurring in practice, likely to be encountered in many fluid dynamic studies where pressure is of interest (e.g. separated flow and bluff body flows). The advection of a Gaussian vortex is taken to serve as a test case for the pressure evaluation procedures. The analytic expression for the velocity field is used to generate synthetic PIV velocity fields, and the corresponding analytic pressure field is used as a reference to validate the pressure field computed from the synthetic PIV velocity fields. In the simulated experiments, the influence of resolution in space and time is considered, as well as noise and spatial filtering caused by PIV, and the effects of 3D (out-of-plane) flow.

#### 3.1 Synthetic flow field

The synthetic flow field consists of a linear combination of a Gaussian vortex and a uniform velocity field in  $x$ -direction,  $U_a$  (corresponding to the advection velocity of the vortex). The flow field relative to the vortex centre is described by the tangential velocity,  $V_\theta$ , in a cylindrical polar coordinate system aligned with the vortex axis and moving with the vortex. The radius where  $V_\theta$  reaches its maximum,  $V_p$ , is defined as the core radius,  $r_c$  (see Fig. 2). The velocity distribution and corresponding pressure distribution (relative to  $p_\infty = 0$ ) are given by

$$V_\theta = \frac{\Gamma}{2\pi r} \left( 1 - e^{-\frac{r^2}{c_\theta}} \right) \quad \text{and} \quad (17)$$

$$p = -\frac{1}{2} \rho V_\theta^2 - \frac{\rho \Gamma^2}{4\pi^2 c_\theta} \left( E_1\left(\frac{r^2}{c_\theta}\right) - E_1\left(\frac{2r^2}{c_\theta}\right) \right), \quad (18)$$

where  $\Gamma$  is the circulation,  $c_\theta = r_c^2/\gamma$ , and  $\gamma = 1.256431$  is a constant to have  $V_p$  at  $r_c$ . The minimum pressure is  $\lim_{r \rightarrow 0} p = -\rho \Gamma^2 \ln 2 / (4\pi^2 c_\theta)$ .  $E_1$  is the exponential integral and is defined as

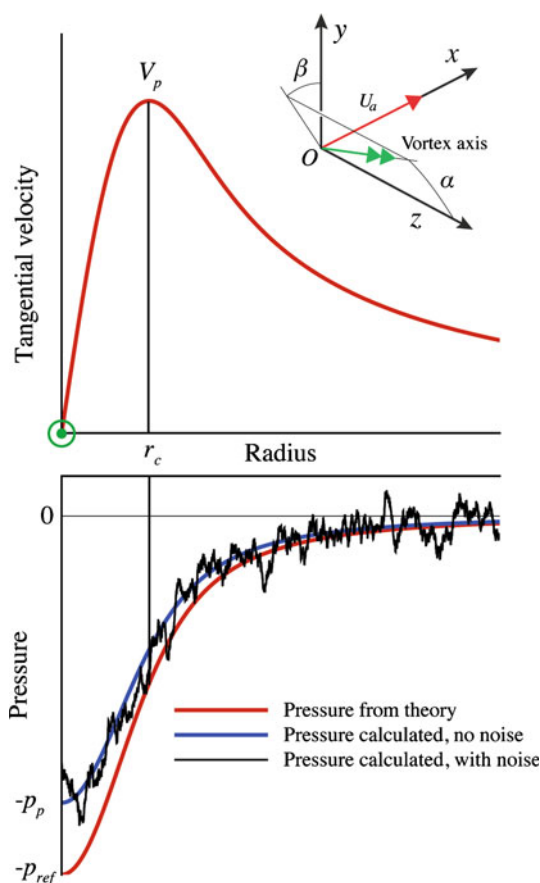


**Fig. 2** Synthetic tangential velocity distribution and corresponding pressure distributions

$$E_1(x) = \int_x^\infty \frac{e^{-t}}{t} dt. \quad (19)$$

3D flow is simulated by tilting the vortex axis at an angle with the  $x$ - $y$ -plane,  $\alpha$ , where the orientation of this angle with respect to the  $y$ -direction is set by a second angle,  $\beta$  (see Fig. 2).

#### 3.2 Numerical implementation

Velocity volumes were created by mapping Eq. 17 onto a cartesian grid (with the vortex axis placed at the centre of the domain) and adding the  $U_a$ , resulting in a grid with values for the  $u$ ,  $v$ , and  $w$  components of velocity and corresponding pressure. The same procedure is followed to create velocity volumes for  $\Delta t$  and  $-\Delta t$ , where the vortex axis is moved the corresponding distance along the advection direction (i.e.  $U_a \Delta t$  and  $-U_a \Delta t$ ).

Nine random noise volumes were created and used in three sets of three (each time one for  $-\Delta t$ ,  $0$  and  $\Delta t$ ). In this way, we assured that the effects of varying parameters are not influenced by the use of different noise volumes (from

case to case) and, by using three sets, we reduce the influence of having a specific response to a single noise volume set.

To account for the filtering effect, PIV has on the velocity field and the noise in the velocity field (see Foucaut et al. 2004), the velocity volume and separate random noise volumes were filtered using a moving-average filter over the interrogation window size (WS) simulating an OF of 75%. After filtering, the volumes were cropped to avoid end-effects of the filtering procedure. The final volumes were  $257 \times 257 \times 9$  points. The thickness of these volumes was sufficient to reconstruct 3D fluid paths for the 3D flow assessment with the Lagrangian approach. For the lower OF values, a subset of this velocity volume was taken. For each case, the noise level was scaled to give the desired root-mean-square (RMS) values,  $\varepsilon_u$ , as a percentage of the maximum (theoretical) velocity occurring in the flow field, in line with PIV practice.

From the velocity fields, the pressure gradient fields were determined using either the Eulerian or Lagrangian approach and subsequently integrated using the Poisson approach, with Dirichlet conditions on the lower side of the domain and Neumann conditions, on the remaining edges, see Fig. 3.

The resulting pressure fields were assessed in two different ways. First, the peak response was determined by taking the ratio of the calculated peak pressure,  $p_p$ , and the peak of the theoretical pressure,  $p_{\text{ref}}$  (see Fig. 2). Second, the noise response,  $\varepsilon_p$ , was determined by taking the (spatial) RMS of the difference between the pressure calculated from the velocity field without noise and the pressure calculated from the velocity field with noise. Each value of the noise response presented is an average of the results of the three sets of noise used.

To investigate the effects of the vortex moving along or across the boundary of the domain (see Fig. 3 for a

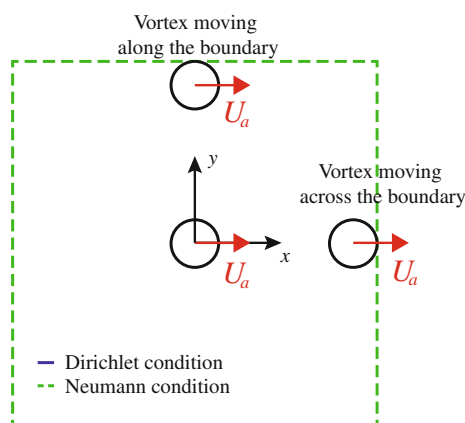


**Fig. 3** Schematic of the computational domain. Indicated are the primary vortex location, the vortex moving along the boundary of the domain and the vortex moving across the boundary of the domain

schematic representation), the vortex centre was placed at different distances from the boundary (ranging from the centre of the domain to the boundary of the domain). The influence is determined by taking the difference between the pressure determination for a stationary vortex and an advecting vortex for each location. The maximum perturbation of all distances is then taken to represent the influence of that advection velocity.

### 3.3 Results

Figure 4 shows the peak and noise responses for different spatial and temporal resolutions. The temporal resolution is split into two contributions, one related to the advection of the vortex (displacement) and one related to the strength of the vortex (rotation). The variations were taken with respect to a noncritical *base-line* as indicated in the caption of Fig. 4.

Figure 4a shows the variation of the peak response with the spatial resolution. The peak response decreases with decreasing spatial resolution. The trend is as expected and is in good agreement with the trend in Fig. 1. The Eulerian and Lagrangian approach perform nearly identical. Increasing the OF only shows significant improvement for the poor resolutions (big WS). The temporal resolution has no influence on the Eulerian approach (Fig. 4b, c). Although this seems in contrast with Eq. 13 (that states the acceleration should not be properly captured), the reason why this does not affect the pressure computation can be understood from the Poisson formulation, which is used to determine the pressure. The flow is 2D, and therefore, the acceleration is completely absent in the 2D part of Eq. 3, the only way that this improper time sampling can affect the results is via the acceleration at the boundaries of the domain. This influence will be covered later. The Lagrangian approach behaves as expected. It is not affected by the advective velocity (Fig. 4b), but is affected by the tangential velocity (Fig. 4c). When plotted with the vortex turnover time,  $V_p \Delta t / 2\pi r_c$  (Fig. 4g), it shows a drop off at  $V_p \Delta t / 2\pi r_c \approx 0.1$ , which is in line with the estimation of the temporal limitation found earlier Eq. 14.

The noise response is unaffected by the spatial resolution, and the OF only has a small influence (Fig. 4d). Figure 4e shows that the noise on the pressure field for the Lagrangian approach increases almost linear with  $U_a$ , which is consistent with Eq. 16, where  $\varepsilon_u$  is defined as a percentage of  $U_{\text{max}}$  in this study. Based on Eq. 15, the noise on the pressure field for the Eulerian approach is predicted to be larger than that for the Lagrangian approach and to increase quadratically with  $U_a$ , which is in good agreement with the trends observed in Fig. 4e. Figure 4f shows an unexpected decreasing trend with increasing tangential velocity. However, it can be shown that  $p_{\text{ref}} \propto V_p^2$  and

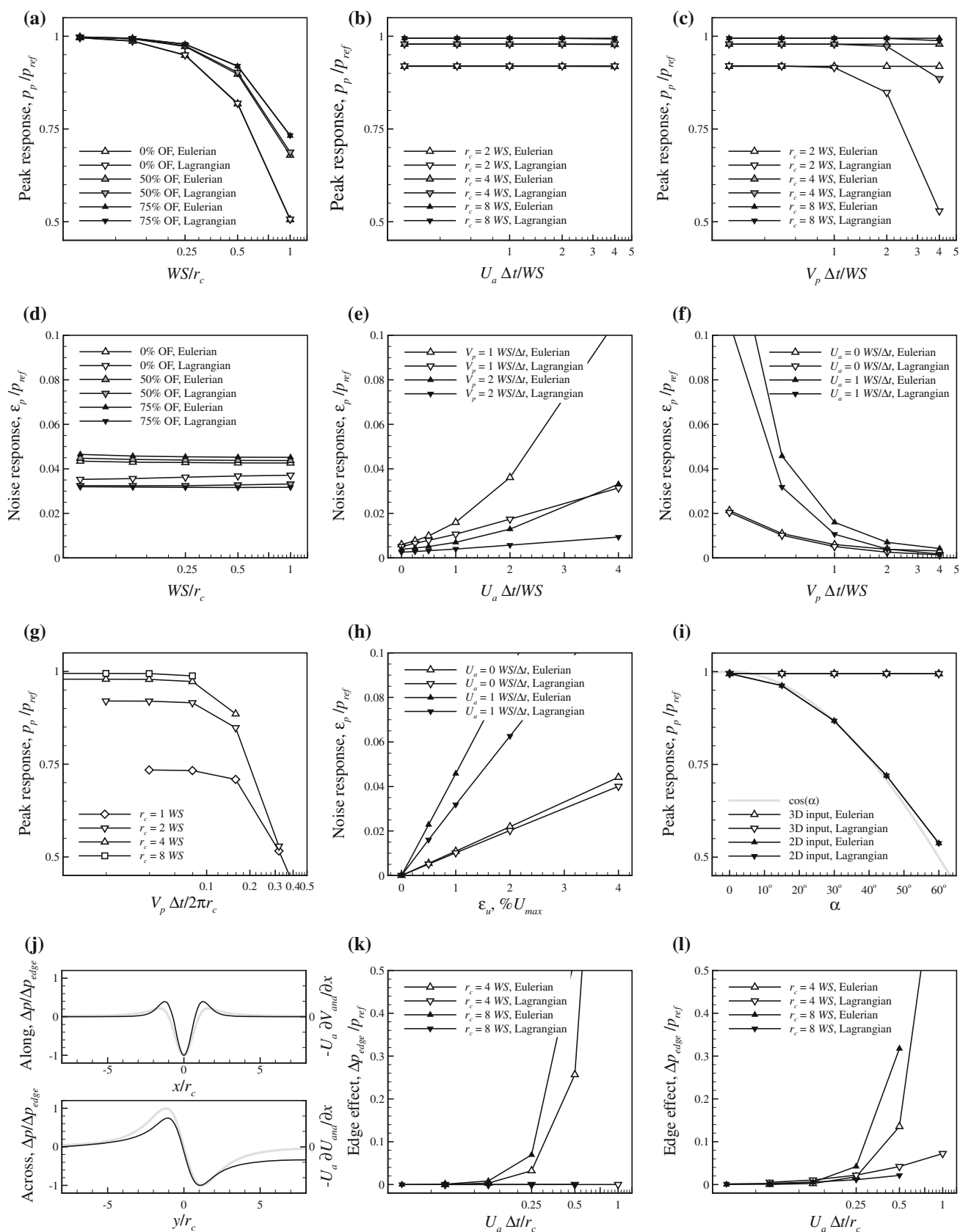




**Fig. 4** Spatial and temporal influences on peak and noise response and edge effects. Unless indicated otherwise:  $U_a = 1WS/\Delta t$ ,  $V_p = 0.5WS/\Delta t$ ,  $r_c = 8WS$ ,  $OF = 75\%$ ,  $\alpha = 0^\circ$ ,  $\beta = 0^\circ$ ; for the noise response:  $\varepsilon_u = 1\%U_{max}$ . **a** Peak response with spatial resolution. **b** Peak response with advective velocity. **c** Peak response with tangential velocity. **d** Noise response with spatial resolution. **e** Noise response with advective velocity. **f** Noise response with tangential velocity. **g** Peak response with vortex turnover time, Lagrangian approach. **h** Noise response with velocity noise. **i** Peak response with angle. **j** Pressure error for the Eulerian approach on the boundary of the domain shown in *black*. Analytic Eulerian acceleration shown in *grey*. *Top* vortex moving along a boundary. *Bottom* vortex moving across a boundary. **k** Maxima of absolute error on the edge for a vortex moving along a boundary. **l** Maxima of absolute error on the edge for a vortex moving across a boundary

therefore  $\varepsilon_p/p_{ref} \propto 1/V_p$ , which explains the trend observed. Figure 4h shows a linear behaviour of the noise on the pressure with increasing noise on the velocity field, which again is in good agreement with Eqs. 15 and 16.

Figure 4i shows the influence of the angle between the vortex axis and the plane normal,  $\alpha$ , for 2D input and 3D input. The 2D input is a subset of the 3D input without the out-of-plane components, which simulates planar or stereo-PIV. The reader should note that although stereo-PIV does give the out-of-plane velocity component, the out-of-plane velocity gradient is needed to make use of the out-of-plane velocity component (see Eq. 3), hence making it equivalent to planar PIV for pressure determination. It is clear that the peak response for the 2D input is very similar to  $\cos(\alpha)$ . No effect associated to  $\beta$  was found.

As indicated earlier, the Eulerian approach is expected to suffer from a temporal limitation on the edges of the domain related to determining the acceleration term of the pressure gradient, see Eq. 13. The maximum perturbation was found to be located at the boundaries, and it decreases with increasing distance from the boundary  $\propto 1/d^2$ , where  $d$  is the distance to the boundary). Figure 4j–l show the results from the assessment of the edge effects. Figure 4j shows the error (black, left scale) introduced along the edge together with the corresponding acceleration (grey, right scale) for a vortex moving along the boundary (top) and for a vortex moving across a boundary (bottom). This shows the error is related to the acceleration. To quantify the influence of  $U_a$  and  $r_c$ , the maximum deviation due to the edge effect is determined and plotted with  $U_a\Delta t/r_c$ . For the Eulerian approach, the edge effect error shows a rapid increase in the error starting at  $U_a\Delta t/r_c \approx 0.2$ , which is in line with Eq. 13, for both the case where the vortex moves along the boundary (Fig. 4k) and the case where the vortex moves across the boundary (Fig. 4l). The Lagrangian approach reacts as expected with only a minor influence for the case where the vortex moves across the boundary (Fig. 4l), which can be attributed to the switch to the forward/backward scheme at the boundary.

### 3.4 Discussion

Although the present evaluation is not directly comparable with the results of the analysis of Charonko et al. (2010), since they did not split the influences of truncation and precision effects, the trends of the peak and noise responses combined match their results.

Successful determination of pressure from PIV data needs to comply with a number of criteria. For both approaches, Eulerian and Lagrangian, the WS should be sufficiently small with respect to the flow structures. A larger OF does increase the quality of the pressure determination, but the effect of OF is less pronounced when the WS is sufficiently small. For WS smaller than  $0.25 r_c$ , the peak response is better than 95%.

Complete 3D velocity measurements are needed to properly capture the pressure in 3D flow, where the impact of not taking the out-of-plane components into account results in a peak response modulation that behaves like  $\cos(\alpha)$ , where  $\alpha$  is the angle of the vortex axis with the measurement plane.

Reducing the measurement noise on the velocity fields directly improves the pressure determination for both approaches.

The Eulerian approach suffers more from measurement noise than the Lagrangian approach, especially when advection velocity is present, and is furthermore limited by the advection of flow structures over the boundary. The time separation between subsequent velocity fields needs to be sufficiently small to correctly capture the acceleration on the boundaries. Time separation should be  $\Delta t < 0.2r_c/U_a$ , which means that the acquisition frequency needs to be 10 times larger than the largest frequency at a given point in the flow (i.e. the Eulerian time scale),  $f_{acq} > 10 \times f_{flow}$  (assuming  $\lambda \approx 2r_c$ ).

The Lagrangian approach is limited by the turnover time of the structures in the flow. The time separation needs to be sufficiently small to correctly capture pressure. The time separation should be  $\Delta t < 0.1 \times 2\pi r_c/V_p$ , which means that the acquisition frequency needs to be larger than 10 times the turnover frequency in the flow (i.e. the Lagrangian time scale),  $f_{acq} > 10 \times f_{turnover}$ .

## 4 Experimental assessment

In previous experiments (de Kat et al. 2009a), the flow around a square-section cylinder was observed to be predominantly 2D along the side of the cylinder and found to have considerable 3D fluctuations in the wake (see also de Kat et al. 2009b). Using similar experimental setups and applying both stereo-PIV and thin-volume tomo-PIV, we will describe the performance of pressure evaluation under

these conditions and how it links in with theoretical performance estimation and the numerical assessment of the preceding sections. Although we have seen that stereo-PIV does not provide more useful information for the pressure determination than planar PIV, it allows assessment of the three-dimensionality of the flow and for this reason, it was used instead of planar PIV. First, we present the results from stereo-PIV to show what accuracy the pressure evaluation can achieve using planar PIV. Secondly, the tomo-PIV results are used to assess the influence of 3D flow effects and to what extent the pressure evaluation improves with inclusion of the 3D flow terms.

#### 4.1 Experimental arrangement and procedure

Experiments were performed in a low-speed, open-jet wind tunnel at the Aerodynamics laboratory at Delft University of Technology. The tunnel outlet has dimensions  $40\text{ cm} \times 40\text{ cm}$ . A square-section cylinder with dimension  $30\text{ mm} \times 30\text{ mm}$  ( $D \times D$ ) and  $34.5\text{ cm}$  in span was fitted with end-plates and positioned in the middle of the free stream. The geometric blockage was  $6.5\%$ . The nominal free-stream velocity,  $U$ , was  $4.7\text{ m s}^{-1}$  (nominal dynamic pressure,  $q = 13.5\text{ Pa}$ ), giving Reynolds number  $Re_D = UD/\nu = 9,500$ . The main vortex shedding frequency was  $f_s = 20\text{ Hz}$ , corresponding to a Strouhal number of  $St = f_s D/U = 0.13$ . The free-stream turbulence intensity was assessed by hot-wire anemometry and was approximately  $0.1\%$ . A summary of the experimental conditions and their uncertainties is given in Table 1.

The cylinder was instrumented with two flush-mounted pressure transducers located in close proximity to midspan of the model to provide reference values for the pressure signals extracted from the PIV data. Figure 5 shows the field-of-view used for the stereo-PIV and tomo-PIV setup as well as the transducer locations. For stereo-PIV, one transducer was located at the bottom and one at the base while for tomo-PIV both transducers are located at the base on either side of the measurement volume. For comparison purposes, pressure measurements were performed with both transducers located at the side of the cylinder on either side of the measurement location.

The pressure transducers, Endevco 8507-C1, have a range of  $1\text{ psi}$  ( $6,895\text{ Pa}$ ) and a typical sensitivity of  $175\text{ mV psi}^{-1}$  ( $25\text{ }\mu\text{V Pa}^{-1}$ ), with a sensitivity change related to temperature of  $<0.2\%$  under current operating conditions. They were calibrated, using a closed system with a U-tube, against a Mensor DPG 2001 (range  $0.5\text{ psi}$ ;  $3,447\text{ Pa}$ , uncertainty  $0.010\%$  full scale). Signal recording was performed using a National Instruments data acquisition system (consisting of: PCI-6250, SCXI-1001, SCXI-1520 and SCXI-1314) operating at  $10\text{ kHz}$  (bandwidth ( $-3\text{ dB}$ ):  $20\text{ kHz}$ ). The resulting noise level was

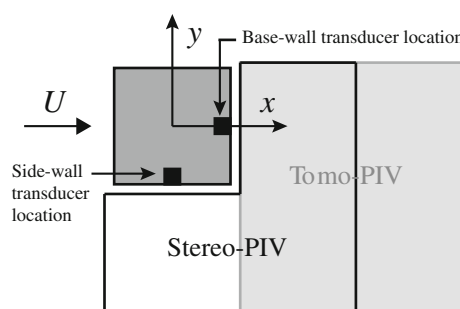


**Fig. 5** Schematic showing the fields-of-view,  $x$ - and  $y$ -directions and pressure transducer locations

$4\text{ }\mu\text{V}_{\text{RMS}}$  resulting in a resolution of  $0.3\text{ Pa}$  (twice the RMS level). The zero drift for each run was  $<2\text{ }\mu\text{V}$ . Unless stated otherwise, the pressure signals are unfiltered (and not corrected for the effects of wind tunnel blockage). The pressure measurement on the side of the model suffered from laser influences. This laser influence was removed by deleting erroneous points in the pressure signal and filling the gaps by interpolation. The signal was subsequently low-pass filtered with a second-order fit (robust Loess) over 25 points. The power spectrum was checked against a pressure measurement without laser interference and was confirmed to be unchanged for frequencies up to  $400\text{ Hz}$ .

A high-repetition-rate PIV system was used to capture the flow. Flow seeding was provided by a Safex smoke generator, which delivered droplets of about  $1\text{ }\mu\text{m}$  in diameter. The measurement plane was illuminated by a Quantronix Darwin-Duo laser system with an average output of  $80\text{ W}$  at  $3\text{ kHz}$  at a wavelength of  $527\text{ nm}$ . The typical energy per pulse was  $16\text{ mJ}$  at  $2.7\text{ kHz}$ . The laser pulse time separation,  $\delta t$ , was  $90\text{ }\mu\text{s}$ . Images were acquired by Photron Fastcam SA1 cameras (two for the stereo setup and four for the tomographic setup) with a  $1,024 \times 1,024$  pixels sensor (pixel-pitch  $20\text{ }\mu\text{m}$ ), recording image pairs at  $2.7\text{ kHz}$ , equipped with Nikon lenses with focal length  $60\text{ mm}$  and aperture set at  $2.8$  (top cameras in tomo-setup at  $5.6$ ). One camera was positioned normal to the image plane. The other cameras were mounted with adapters such that the Scheimpflug criterion was met. A total of  $2,728$  image pairs, spanning just over  $1\text{ s}$ , was captured for both configurations. Synchronization between the cameras, laser, and image acquisition was accomplished by a LaVision programmable unit in combination with a high-speed controller, both controlled through DaVis 7.2 software. Particle image pairs were processed using DaVis 7.4 software. Self-calibration for both the stereo- and tomo-PIV was performed, see Wieneke (2005, 2008). Particle images were preprocessed by subtracting the time minimum and applying a  $3 \times 3$  gaussian filter. Vector fields were processed with a median test (see e.g. Westerweel and Scarano 2005) combined with a multiple correlation peak

**Table 1** Experimental conditions

Variable	Value	Uncertainty (%)
Free-stream velocity, $U$	4.7 m s <sup>-1</sup>	±2
Free-stream turbulence intensity	0.1% $U$	–
Tunnel dimension	400 mm	–
Cylinder dimension, $D$	30 mm	–
Geometric blockage	6.5%	–
Cylinder span	345 mm	–
Reynolds number, $Re_D$	9,500	±2
Dynamic pressure, $q$	13.5 Pa	±2
Vortex shedding frequency, $f_s$	20 Hz	±1
Strouhal number, $St$	0.13	±2

**Table 2** Main PIV settings

	Stereo-PIV	Tomo-PIV
Number of cameras	2	4
Lenses	Nikon 60 mm	Nikon 60 mm
Aperture setting, $f_\#$	2.8	2.8 and 5.6
Angle between cameras	32°	30° × 30°
Digital resolution	15.7 pix mm <sup>-1</sup>	14.3 pix mm <sup>-1</sup>
Acquisition frequency, $f_{acq}$	2.7 kHz	2.7 kHz
Laser sheet thickness	1 mm	4 mm
Laser pulse time sep., $\delta t$	90 μs	90 μs
Velocity field time sep., $\Delta t$	370 μs	370 μs
Initial interrogation area	32 × 32 pix	32 × 32 × 32 pix
Final interrogation area	16 × 16 pix	16 × 16 × 16 pix
Overlap factor	50%	50%
Vector field size	118 × 125	99 × 110 × 7

check. Remaining spurious vectors were removed and replaced using linear interpolation. The total number of spurious vectors was <2% for both data-sets.

An overview of the main PIV settings used in this investigation is given in Table 2. For the stereo-PIV, the field-of-view (FOV) was captured with a digital resolution of 15.7 pix mm<sup>-1</sup>. The laser light sheet thickness was approximately 1 mm. The final interrogation WS was varied between 16 × 16 pixels and 128 × 128 pixels and the OF between 0 and 75% resulting in vector grids of 236 × 250 vectors to 14 × 15 vectors (after cropping), for 16 × 16 pixels with 75% OF and 128 × 128 pixels with 50% OF, respectively. For the tomo-PIV, the illuminated volume was 70 mm × 70 mm × 4 mm. It was captured with a digital resolution of 14.3 pix mm<sup>-1</sup>. The final interrogation volume size of 16 × 16 × 16 voxels with an OF of 50% gave a vector grid of 99 × 110 × 7 vectors (after cropping) with vector spacing of 0.56 mm.

The in-plane pressure gradient was determined using either the Lagrangian or the Eulerian formulation. The pressure field was subsequently obtained by the Poisson integration approach with a Dirichlet condition on the

lower edge of the domain and Neumann conditions on the remaining edges.

The estimated error on the velocity field expressed as a RMS uncertainty was determined using a linear uncertainty-propagation analysis, taking the free-stream particle displacement and the error on the particle displacement. Based on results from undisturbed flow for the stereo-PIV setup (with the model removed), the RMS error on the in-plane particle displacement was found to be 0.1 pixel. The error on the velocity was found to be  $\sigma_u/U \approx 1.5\%$ , where  $\sigma_u$  is the RMS uncertainty on the velocity and  $U$  is the free-stream velocity.

## 4.2 Data analysis

Pressure signal time series are extracted from the pressure fields obtained from PIV. The (temporal) mean,  $\bar{p}$  and  $\bar{p}_{ref}$ , and (temporal) RMS,  $\sigma_p$  and  $\sigma_{ref}$ , are determined of the PIV pressure signal and pressure transducer signal, respectively. Consecutively, the mean response  $\bar{p}/\bar{p}_{ref}$  and RMS response  $\sigma_p/\sigma_{ref}$  are determined. Next, the temporal correlation coefficient between the pressure signals from PIV and the pressure transducers is determined using

$$\text{Corr. coeff.} = \frac{\text{cov}(p, p_{ref})}{\sigma_p \sigma_{ref}} \quad (20)$$

where  $\text{cov}(p, p_{ref})$  is the covariance between the two pressure signals.

Power spectral densities are determined for the main PIV cases and their corresponding pressure transducer signals by averaging the spectra from seven blocks with 50% overlap. Finally, we determine the coherence between the pressure signal time series from PIV and the pressure signal time series from the pressure transducers (also using seven blocks with 50% overlap). We are only interested in comparing the signals as they are (without any phase-lag), and therefore, we take the real part of the coherence and define this to be the dynamic correlation. The dynamic correlation represents the correlation coefficient per frequency component.

$$\text{Dyn. corr.} = \Re \left( \frac{C_{pp_{ref}}}{\sqrt{P_{pp}} \sqrt{P_{ref_{ref}}}} \right) \quad (21)$$

where  $C_{pp_{ref}}$  is the co-spectrum of the pressure from PIV and the pressure from the pressure transducer, and  $P_{pp}$  and  $P_{ref_{ref}}$  are the power spectral densities of the pressure from PIV and the pressure transducer, respectively.

## 4.3 Results

### 4.3.1 Stereo-PIV

A typical result for stereo-PIV is shown in Fig. 6, which illustrates the relation between separated high-vorticity

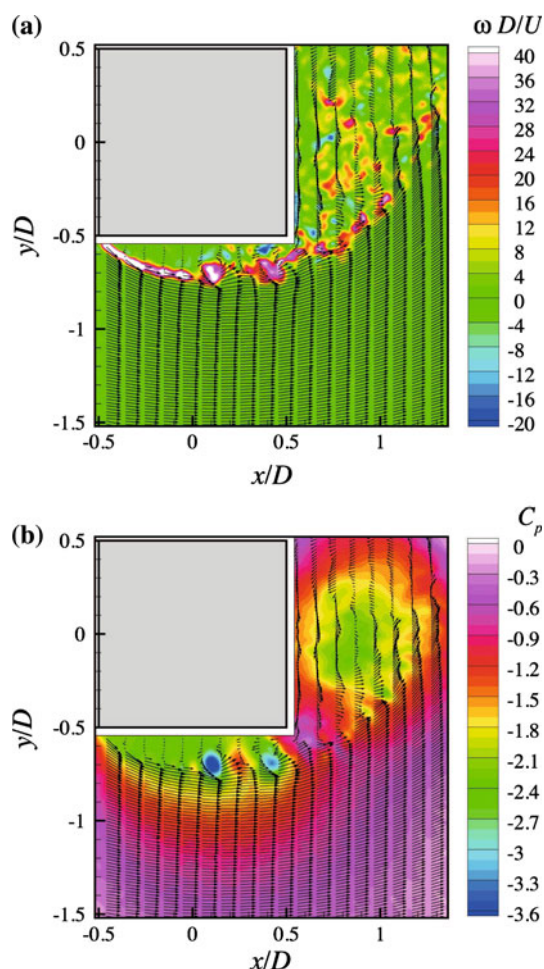


**Fig. 6** Example of the stereo-PIV results. Each sixth vector in  $x$ -direction is shown. **a** Vorticity field. **b** Pressure field

regions and low-pressure regions, especially apparent in the separated shear layer along the bottom side of the square cylinder. In the wake, the relatively large low-pressure region can be associated to the formation of a Von Kármán vortex, which is more clearly visible when considering phase-averaged results (see e.g. van Oudheusden et al. 2005; de Kat et al. 2010).

Figure 7 shows pressure signal time series extracted from the pressure fields derived from stereo-PIV using the Eulerian approach compared to the pressure transducer signals. The signals for the side-wall (Fig. 7, top) are in good agreement, whereas the signals for the base-wall (Fig. 7, bottom) show a fair agreement. To quantify the agreement between the signals and to investigate the effects of spatial and temporal resolution, the mean and RMS responses as well as the cross-correlation values with respect to the pressure transducer signal are determined and shown in Figs. 8 and 9 for the side and base-wall, respectively. As a comparative reference, values determined from pressure transducers on either side of the PIV

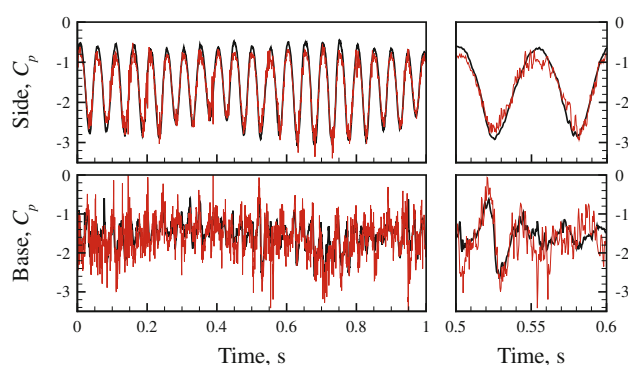


**Fig. 7** Pressure signal time-series from stereo-PIV. The pressure signal from PIV is shown in *red*. The pressure transducer signal is shown in *black*. *Top* side-wall signals. *Bottom* base-wall signals. *Left* full time series. *Right* 0.1 s subset of the time series

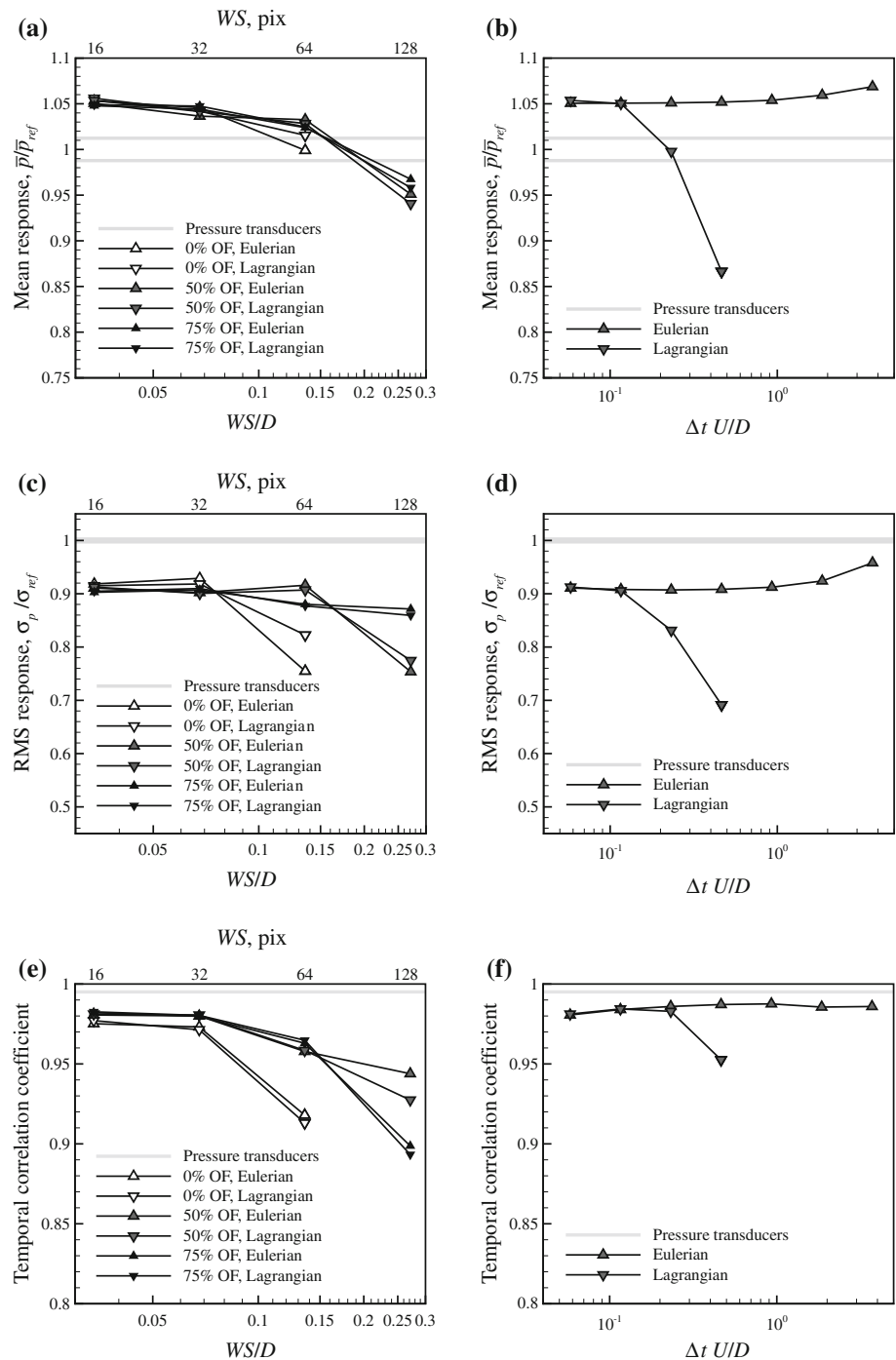
domain are indicated by grey lines. As the two transducers do not produce entirely identical signals, the mean and RMS responses of these transducers are compared with each other, taking each as the reference for the other, which results in two values for the mean and RMS response and one for the correlation value.

Figure 8a, c, and e show the influence of the spatial resolution on the side-wall pressure signal obtained from stereo-PIV. The mean response is within 5% for all WS and OF. The RMS response together with the temporal correlation coefficient show that the larger WS are modulating the signal, reducing the temporal correlation coefficient to below 0.95. For the higher spatial resolutions (small WS), there is no difference between the 50 and 75% OF. For resolutions higher than  $WS/D \approx 0.1$ , there is little change, this is in line with the size of the structures observed next to the side of the square cylinder, which are of order  $0.1 D$ . No apparent difference between the Eulerian and Lagrangian approach can be distinguished.

Figure 8b, d, and f show the influence of the temporal resolution on the side-wall pressure signal from stereo-PIV. The Eulerian approach shows almost a constant response across the entire range covered, whereas the Lagrangian approach drops off at  $\Delta t U/D \approx 0.2$ . The results for the Eulerian approach agree with the findings from the assessment on the synthetic flow field, and there is no sign of the limit estimated in Eq. 13, since there are no vortices moving along or across boundaries near the side-wall pressure transducer location. The vortex turnover time was estimated to verify to what extent the current results agree with the findings from the assessment on the synthetic flow field and the theoretical estimate in Eq. 14. The structures next to the side of the square cylinder (Fig. 6 shows two structures that are stronger than average) have an average maximum vorticity of around  $30 U/D$ , resulting in a vortex turnover time (assuming a Gaussian vortex) of  $\Delta t U/D \approx 0.3$ , which shows that the drop off observed is in



**Fig. 8** Spatial and temporal influences on the side-wall pressure signal from stereo-PIV. Unless indicated otherwise, settings are as listed in Table 2. **a** Mean response with spatial resolution. **b** Mean response with temporal resolution. **c** RMS response with spatial resolution. **d** RMS response with temporal resolution. **e** Temporal correlation coefficient with spatial resolution. **f** Temporal correlation coefficient with temporal resolution



line with what is expected from the assessment on the synthetic flow field and the theoretical considerations.

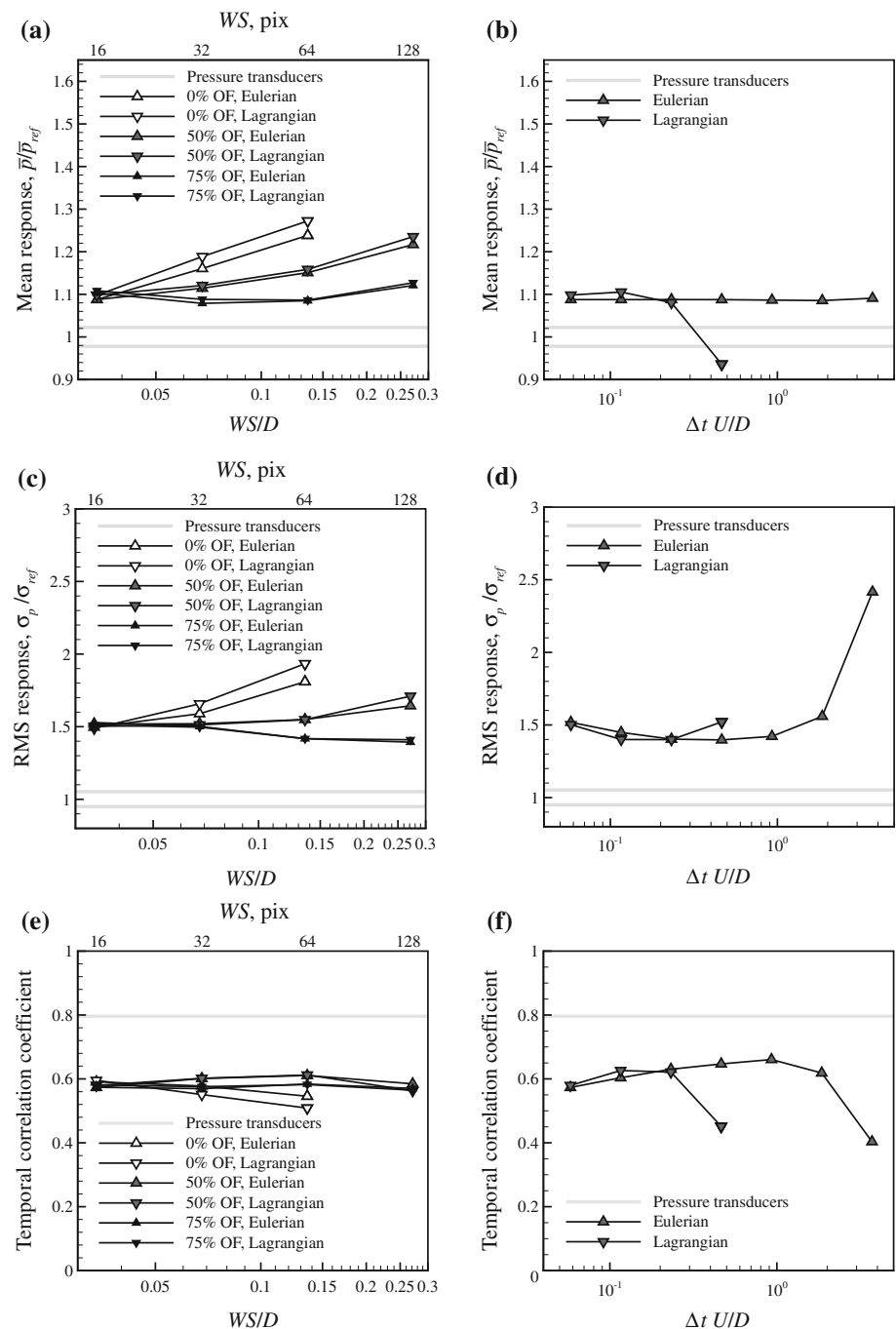
Figure 9a, c, and e show the influence of the spatial resolution on the base-wall pressure signal from stereo-PIV. The mean response converges to approximately a 10% difference for all OF for  $WS = 16$  pix. The RMS response also converges to similar values for all OF, but overestimating the RMS by 50%. The temporal correlation coefficients are all around a value of 0.6. The structures

observed next to the base of the square cylinder go down to sizes of order  $0.05 D$ , which would explain the mean and RMS response to be similar for all OF for  $WS/D < 0.05$ .

Figure 9b, d, and f show the influence of the temporal resolution on the base-wall pressure signal from stereo-PIV. The mean response for the Eulerian approach is almost constant across the entire range covered, whereas the RMS response and temporal correlation coefficient



**Fig. 9** Spatial and temporal influences on the base-wall pressure signal from stereo-PIV. Unless indicated otherwise, settings are as listed in Table 2. **a** Mean response with spatial resolution. **b** Mean response with temporal resolution. **c** RMS response with spatial resolution. **d** RMS response with temporal resolution. **e** Temporal correlation coefficient with spatial resolution. **f** Temporal correlation coefficient with temporal resolution



show a departure at  $\Delta t U/D \approx 3$ . The shedding frequency gives us two vortices per cycle (one clockwise and one counter-clockwise) resulting in  $\Delta t U/D = 1/(2St) \approx 4$ , which means that the small vortices seem to have no effect on the Eulerian approach, whereas the large Von Kármán shedding does. The results for the Lagrangian approach drop off at  $\Delta t U/D \approx 0.3$ . The structures next to the base of the square cylinder (see Fig. 6) have an average maximum vorticity of around  $15U/D$ , resulting in a vortex turnover time (assuming a Gaussian vortex) of  $\Delta t U/D \approx 0.6$ , which shows the drop off observed is again in line with the

assessment on the synthetic flow field and the theoretical considerations.

The results from stereo-PIV for the base show some other more subtle variations, but the fact that the flow is 3D in the wake makes it impossible to make further statements about the performance without including the out-of-plane terms.

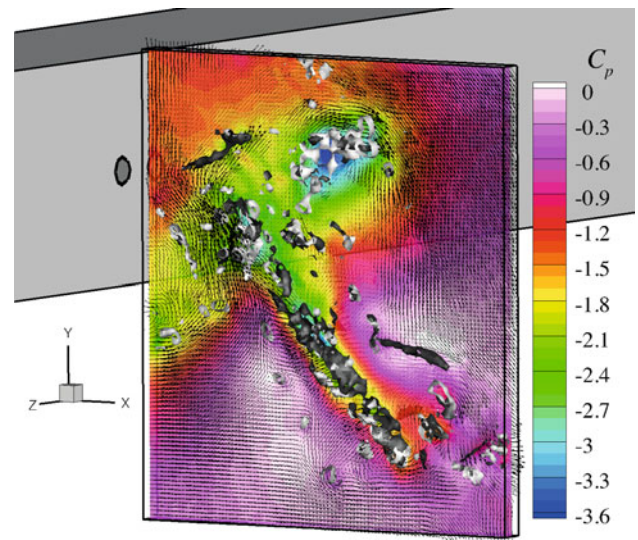
#### 4.3.2 Tomo-PIV

The results for the base-wall pressure signal from stereo-PIV lack the full 3D information needed for proper

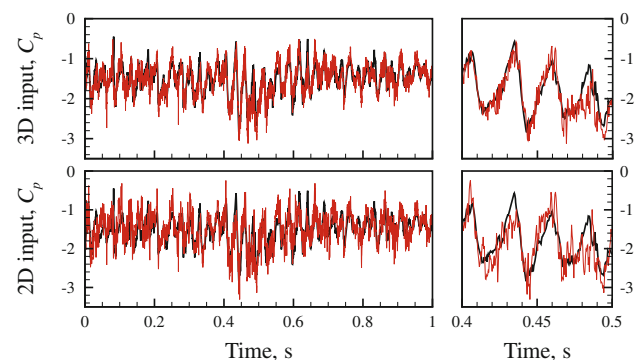
pressure determination in a 3D flow. To assess the effect of the omission of the 3D terms, tomo-PIV experiments were performed. Since the main difference between the Eulerian and Lagrangian approach seems to be related to the temporal resolution, we focus on one combination of interrogation volume (3D equivalent of WS) and OF ( $16 \times 16 \times 16$  pixels and 50% OF) and only investigate the influence of temporal resolution. Figure 10 shows an example of the results from tomo-PIV. Isosurfaces indicate the out-of-plane and in-plane vorticity. Together with the vectors that are plotted in 3D, they give a good indication of the 3D nature of the flow in the wake. The mid-plane is colour-flooded with the corresponding pressure field. The low-pressure regions are located near the regions of high in-plane and/or out-of-plane vorticity, showing that the pressure field is influenced by the 3D nature of the flow.

Figure 11 shows the pressure signal time series from tomo-PIV using the Eulerian approach compared with the pressure transducer that is depicted in Fig. 10. Both results with input of the full 3D information (Fig. 11, top) and a 2D subset (Fig. 11, bottom) of the tomo-PIV data are shown. The difference between these results indicates the influence of adding or omitting the extra 3D information. They both seem to have a good agreement with the pressure transducer signal, where the results with the 3D input seem to be in better agreement. To quantitatively assess the performance of pressure determination and to compare different methods, the mean response, the RMS response, and the temporal correlation coefficients are determined for different time separations,  $\Delta t$ , and shown in Fig. 12. Due to out-of-plane motion in combination with a limited thickness of the volume, only the smallest time separation gave results for the 3D Lagrangian approach. Even for this case, the pressure gradient at some points could not be determined, i.e. the fluid path could not be reconstructed due to large values of the out-of-plane velocity. If larger time separations are needed, the volume thickness should be increased.

The results for the base-wall pressure signal for 2D input show the same trends as the results from stereo-PIV (cf. Fig. 9). The main difference is in the values of the responses. The results of the 2D input from tomo-PIV are better than the results from stereo-PIV with values under 5% for the mean response (10% for stereo-PIV), 20–30% difference for the RMS response (50% for stereo-PIV) and a cross-correlation value of up to 0.7 (0.65 for stereo-PIV). This improvement suggests that tomo-PIV is better than stereo-PIV at capturing the in-plane velocity components in 3D flow. A possible explanation for this improvement is that tomo-PIV can also adapt (as it is an iterative process) to an out-of-plane gradient, whereas stereo-PIV (and planar PIV as well) can only adapt to the in-plane gradient. Another possible factor is the error introduced by



**Fig. 10** Example of the tomo-PIV results. Isosurfaces of out-of-plane vorticity are shown in *light grey*,  $\omega_z = 15D/U$ . Isosurfaces of in-plane vorticity are shown in *dark grey*,  $\sqrt{\omega_x^2 + \omega_y^2} = 20D/U$ . 3D vectors are shown in the plane where pressure is determined



**Fig. 11** Base-wall pressure signal time series from Tomo-PIV, Eulerian approach. The pressure signal from PIV is shown in *red*. The pressure transducer signal is shown in *black*. *Top* 3D input. *Bottom* 2D input. *Left* full time series. *Right* 0.1 s subset of the time series

perspective in stereo-PIV, which becomes worse for small ratios of the WS with the laser light sheet thickness (see Raffel et al. 2007, in the current study a WS of  $16 \times 16$  pixels corresponds to a ratio of approximately 1). The 2D Lagrangian approach drops off at  $\Delta t U/D \approx 0.3$ . The results for the Eulerian approach show an increase in RMS response value similar to the noise response with increasing advective velocity as shown in Fig. 4e.

The most interesting difference between the 2D and 3D input results can be seen in the temporal correlation coefficients, Fig. 12c. From  $\Delta t U/D \approx 0.4$  and higher temporal resolutions (smaller  $\Delta t$ ) the 3D input shows a significant increase in temporal correlation coefficient over the 2D

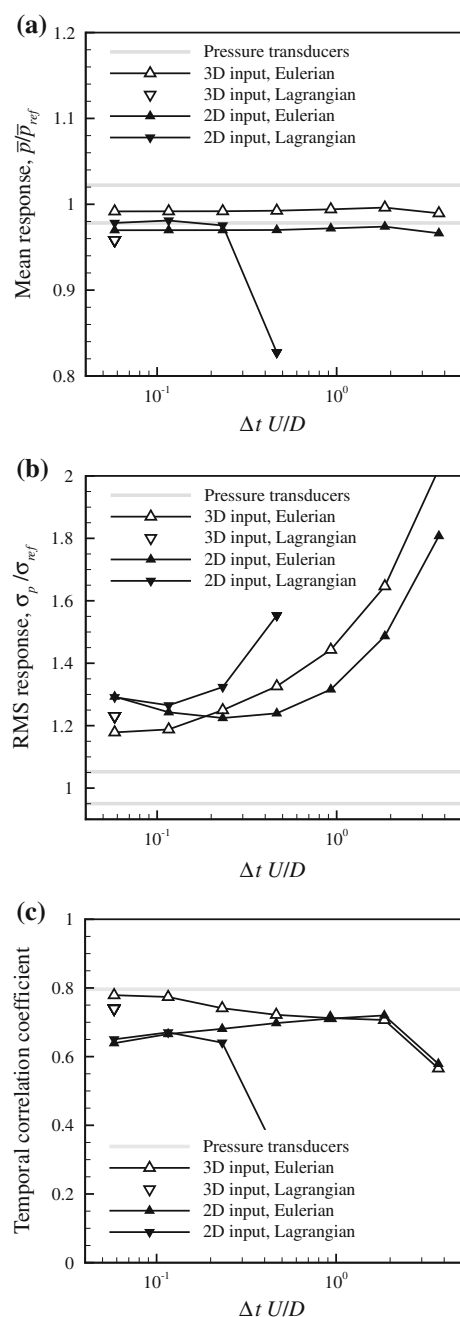


**Fig. 12** Temporal influences on the base-wall pressure signal from tomo-PIV. Unless indicated otherwise, settings are as listed in Table 2. **a** Mean response. **b** RMS response. **c** Temporal correlation coefficient

input. Also, the Lagrangian approach shows the same increase for the single case where the 3D results could be determined. This increase in correlation can be explained by the fact that the temporal resolution is now sufficient to describe the motion of smaller 3D structures in the wake, which results in a better correlation for the 3D input, but a worse correlation for the 2D input. For the 2D input, the partial description of the small 3D structures is experienced as noise.

#### 4.3.3 Spectral assessment

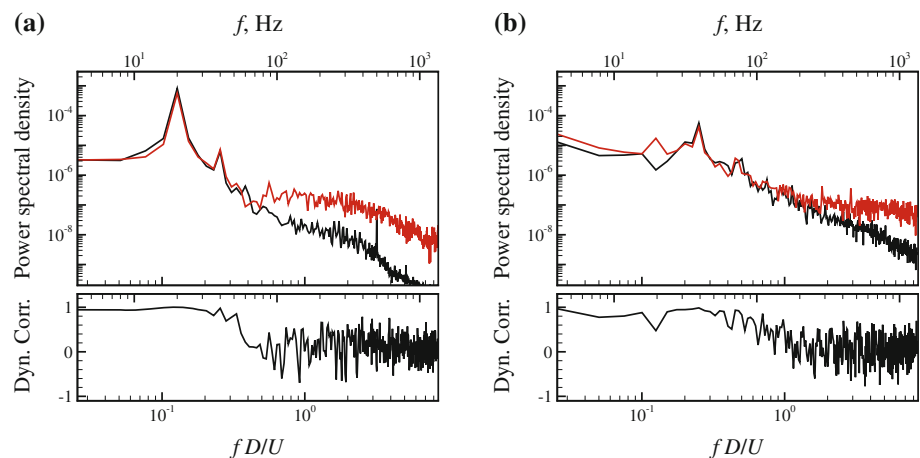
To assess the range of frequencies that can be captured with pressure determination, power spectral density of the side-wall and base-wall pressure signals obtained from stereo-PIV and tomo-PIV, respectively, (using the Eulerian approach) are determined for the main test cases (see Table 2) and shown in Fig. 13, top) alongside with the power spectral density of the corresponding pressure transducer signal. The dynamic correlation between the PIV and corresponding pressure transducer signals are shown in Fig. 13, bottom). The side-wall pressure shows a pronounced peak at the shedding frequency (20 Hz), while the base pressure displays a slightly less pronounced peak at double the shedding frequency. The stereo-PIV power spectral density for the side-wall shows an excellent agreement up to approximately 80 Hz where the pressure from PIV spectrum departs abruptly from that of the pressure transducer. The dynamic correlation also shows an abrupt drop from near unity to zero in the range 50–70 Hz. This abrupt difference in amplitude (energy) and correlation can be attributed to the small 3D component in the shear layer. De Kat et al. (2009a) show that even though the flow along the side of the cylinder is predominantly 2D, the shear layer has significant 3D fluctuations near the trailing edge of the model, which are caused by the shear layer undergoing transition. The shear layer has a frequency in the range of  $10^2$ – $10^3$  Hz, which coincides with the region where the two spectra differ. The tomo-PIV power spectral density for the base-wall show an excellent agreement up to 200–300 Hz. The dynamic correlation shows that there is good correlation between the signals before it drops to 0 around 200 Hz. The small differences in the low frequency range can be ascribed to the limited number of cycles to get a good converged spectrum at these frequencies.

#### 4.4 Discussion

Although the PIV measurements were not capable to capture all the structures in the flow due to the limitation in spatial resolution, the results support the guidelines given in Sect. 3.

With respect to the spatial resolution, good results (mean response within 5%, RMS response within 10% and the temporal correlation coefficient  $>0.9$ ) are obtained for  $WS/D < 0.2$ , see the experimental result in Fig. 8a, c, and e). The size of the large flow structure along the side of the cylinder can be approximated by the section dimension,  $\lambda_x \approx D$ , and the size of the flow structure in the test on the synthetic flow field can be approximated by twice the vortex core radius,  $\lambda_x \approx 2r_c$ . Then, the results from the theoretical test in Sect. 3 give a peak response of 0.9

**Fig. 13** Power spectral density plots (top) and dynamic correlation plots (bottom) for the main PIV cases (see Table 2). The spectrum for pressure from PIV is shown in red. The spectrum for the pressure transducer is shown in black. **a** Side-wall, stereo-PIV. **b** Base-wall, Tomo-PIV



for  $WS/\lambda_x \approx 0.25$ . This suggests that for good pressure results from PIV, there need to be at least four to five  $WS$  covering the flow structure.

The spectral results for the base-wall pressure signal from tomo-PIV show a loss of coherence and a change of spectral power for  $f_{\text{flow}} > 200\text{--}300$  Hz. This corresponds to  $f_{\text{acq}}/f_{\text{flow}} > 13.5\text{--}9$ , which is in good agreement with the requirement on the temporal resolution,  $f_{\text{acq}}/f_{\text{flow}} > 10$ .

For the current flow problem, where the advective influences are small compared to the strength of the vortices, the restrictions on the Lagrangian approach (reconstruction of the fluid path) were found to be more limiting than the restrictions on the Eulerian approach (accurate estimation of the acceleration, especially near the domain edges).

The differences observed between the Eulerian approach, Lagrangian approach, and the reference pressure are due to influences of 3D flow (for planar measurements) and spatial and temporal resolution, not due to measurement noise. Estimating  $U_a$  and  $V_p$  to be in the order of the free-stream velocity,  $U (\approx 2WS/\Delta t)$ , then, based on the analysis in Sect. 3 and  $\sigma_u/U \approx 1.5\%$ , the effect of noise is expected to be lower than 2%, which is well below the differences found due to the spatial and temporal resolution (and 3D flow).

## 5 Conclusions

The operating principles of obtaining pressure from PIV using an Eulerian and Lagrangian approach have been described together with theoretical considerations on its performance. These considerations were found to be in line with the result from assessment on a synthetic flow field, consisting of an advecting vortex. From these results, guidelines are proposed considering the temporal and spatial resolution needed to correctly capture the instantaneous pressure from PIV. It was found for both methods that the  $WS$  needs to be at least 5 times smaller than the flow structure ( $\lambda_x$ ). For both methods, it holds that the

acquisition frequency needs to be 10 times higher than the frequency in the flow, where this frequency for the Eulerian approach is related to the Eulerian time scales and for the Lagrangian approach to the Lagrangian time scales.

Stereo-PIV and thin-volume tomo-PIV measurements, considering the flow around a square cylinder, were performed to provide experimental verification, with surface-transducer pressure data for validation. Subsequent analysis of the results showed that accurate pressure determination from PIV is possible in both 2 and 3D flows. The experimental results support the guidelines derived from the theoretical considerations and the assessment on a synthetic flow field. The pressure at the side-wall of the square cylinder could be determined from stereo-PIV data with a difference with respect to the pressure transducers of 5% in the mean, 10% on RMS, and with a correlation value of 0.98. The pressure at the base-wall of the square cylinder could be determined from tomo-PIV data with a difference with respect to the pressure transducers of 2% in the mean, 20% on RMS, and with a correlation value of 0.8 (the correlation value between the pressure transducers on either side of the volume was also 0.8).

**Acknowledgments** The authors would like to thank X. Liu and J. Katz from Johns Hopkins University for their hospitality during the research visit of R. de Kat and for the use of their omnidirectional integration scheme. The authors would like to thank the reviewers for their helpful comments and suggestions. The authors would like to thank F. Scarano for all the comments and discussions.

**Open Access** This article is distributed under the terms of the Creative Commons Attribution Noncommercial License which permits any noncommercial use, distribution, and reproduction in any medium, provided the original author(s) and source are credited.

## References

- Baur T, Köngeter J (1999) PIV with high temporal resolution for the determination of local pressure reductions from coherent turbulence phenomena. In: 3rd International workshop on particle image velocimetry, Santa Barbara, 16–18 September, pp 1–6

- Charonko J, King CV, Smith BL, Vlachos PP (2010) Assessment of pressure field calculations from particle image velocimetry measurements. *Meas Sci Technol* 21:1–16
- Christensen K, Adrian RJ (2002) Measurement of instantaneous Eulerian acceleration fields by particle image accelerometry: method and accuracy. *Exp Fluids* 33(6):759–769
- de Kat R, van Oudheusden BW, Scarano F (2008) Instantaneous planar pressure field determination around a square-section cylinder based on time-resolved stereo-PIV. In: 14th International symposium on applications of laser techniques to fluid mechanics, Lisbon, 7–10, July, pp 1–11
- de Kat R, van Oudheusden BW, Scarano F (2009a) Instantaneous pressure field determination around a square-section cylinder using time-resolved stereo-PIV. In: 39th AIAA fluid dynamics conference, San Antonio
- de Kat R, van Oudheusden BW, Scarano F (2009b) Instantaneous pressure field determination in a 3D flow using time-resolved thin volume tomographic PIV. In: 8th International symposium on particle image velocimetry, Melbourne, pp 1–4
- de Kat R, Humble RA, van Oudheusden BW (2010) Time-resolved PIV study of a transitional shear layer around a square cylinder. In: Proceedings of the IUTAM symposium on bluff-body wakes and vortex induced vibrations, Capri
- Elsinga GE, Scarano F, Wieneke B, van Oudheusden BW (2006) Tomographic particle image velocimetry. *Exp Fluids* 41(6):933–947
- Foucaut J, Stanislas M (2002) Some considerations on the accuracy and frequency response of some derivative filters applied to particle image velocimetry vector fields. *Meas Sci Technol* 13(7):1058–1071
- Foucaut J, Carlier J, Stanislas M (2004) PIV optimization for the study of turbulent flow using spectral analysis. *Meas Sci Technol* 15:1046–1058
- Fujisawa N, Tanahashi S, Srinivas K (2005) Evaluation of pressure field and fluid forces. *Meas Sci Technol* 16:989–996
- Fujisawa N, Nakamura Y, Matsuura F, Sato Y (2006) Pressure field evaluation in microchannel junction flows through PIV measurement. *Microfluid Nanofluid* 2(5):447–453
- Gurka R, Liberzon A, Hefetz D, Rubinstein D, Shavit U (1999) Computation of pressure distribution using PIV velocity data. In: 3rd International workshop on particle image velocimetry, Santa Barbara, 16–18 September, pp 1–6
- Hosokawa S, Moriyama S, Tomiyama A, Takada N (2003) PIV measurement of pressure distributions about single bubbles. *J Nucl Sci Technol* 40(10):754–762
- Jakobsen M, Dewhurst T, Greated C (1997) Particle image velocimetry for predictions of acceleration fields and force within fluid flows. *Meas Sci Technol* 8:1502–1516
- Kline SJ, McClintock FA (1953) Describing uncertainties in single-sample experiments. *Mech Eng* 75:3–8
- Liu X, Katz J (2006) Instantaneous pressure and material acceleration measurements using a four-exposure PIV system. *Exp Fluids* 41(2):227–240
- Noca F, Shiels D, Jeon D (1999) A comparison of methods for evaluating time-dependent fluid dynamic forces on bodies, using only velocity fields and their derivatives. *J Fluid Struct* 13(5):551–578
- Raffel M, Willert CE, Wereley ST, Kompenhans J (2007) Particle image velocimetry: a practical guide, 2nd edn. Springer, Heidelberg
- Schrijer FFIJ, Scarano F (2008) Effect of predictor–corrector filtering on the stability and spatial resolution of iterative PIV interrogation. *Exp Fluids* 45(5):927–941
- Schröder A, Geisler R, Elsinga GE, Scarano F, Dierksheide U (2008) Investigation of a turbulent spot and a tripped turbulent boundary layer flow using time-resolved tomographic PIV. *Exp Fluids* 44(2):305–316
- Stern F, Muste M, Beninati ML, Eichinger WE (1999) Summary of experimental uncertainty assessment methodology with example. Iowa Institute of hydraulic research technical report no 406, pp 1–41
- van Oudheusden BW (2008) Principles and application of velocimetry-based planar pressure imaging in compressible flows with shocks. *Exp Fluids* 45(4):657–674
- van Oudheusden BW, Scarano F, van Hinsberg NP, Watt D (2005) Phase-resolved characterization of vortex shedding in the near wake of a square-section cylinder at incidence. *Exp Fluids* 39(1):86–98
- van Oudheusden BW, Scarano F, Roosenboom EWM, Casimiri EWF, Souverein LJ (2007) Evaluation of integral forces and pressure fields from planar velocimetry data for incompressible and compressible flows. *Exp Fluids* 43(2):153–162
- Violato D, Moore P, Scarano F (2010) Lagrangian and Eulerian pressure field evaluation of rod-airfoil flow from time-resolved tomographic PIV. *Exp Fluids* (online first)
- Westerweel J, Scarano F (2005) Universal outlier detection for PIV data. *Exp Fluids* 39(6):1096–1100
- Wieneke B (2005) Stereo-PIV using self-calibration on particle images. *Exp Fluids* 39(2):267–280
- Wieneke B (2008) Volume self-calibration for 3D particle image velocimetry. *Exp Fluids* 45(4):549–556
- Williamson CHK (1996) Vortex dynamics in the cylinder wake. *Annu Rev Fluid Mech* 28(1):477–539